Dynamic Modeling and Control of Biologically Inspired Vortex Ring Thrusters for Underwater Robot Locomotion

Michael Krieg, *Student Member, IEEE*, and Kamran Mohseni, *Member, IEEE*

***Abstract*—A new type of underwater thruster was designed to provide high-accuracy, low-speed maneuvering to underwater robots. Located internal to the vehicle surface, these thrusters have a minimal effect on the forward-drag profile of the vehicle. These thrusters, whose inspiration comes from the natural propulsion of cephalopods and jellyfish, generate control forces by successive ingestion and expulsion of jets of water from a cavity mounted in the hull of the vehicle. The jetting process has no net mass flux but results in a positive momentum flux. A time-dependent thrust model was developed, which predicted the thruster dynamics as a function of time, actuation frequency, and thruster-driving parameters. A linear transfer-function model was developed to approximate both the thruster and vehicle dynamics, which led to maneuver categorization into three regimes: *Cruising*, *Docking*, and *Transition*. The predicted frequency response was verified through hybrid simulation to be accurate for predicting general trends and cutoff frequency.**

***Index Terms*—Autonomous underwater vehicle (AUV), control, maneuvering, propulsion, vortex ring.**

I. INTRODUCTION

ACCURATE maneuvering and control of underwater vehicles presents a difficult multifaceted control problem. The dynamics of typical thrusters and control surfaces are highly nonlinear, which makes controlling the vehicle difficult in the absence of any other factors. On top of which, the environment these vehicles operate in induces hydrodynamic forces, which are poorly modeled, highly dependent on relative vehicle velocity and, above all, cluttered with ocean-current disturbances. In order to reject these disturbances, the vehicle's maneuver systems must be capable of instantaneous uncoupled corrective propulsion [1].

Typical underwater vehicles with active propulsion fall into one of two categories. The first, which is termed the "torpedo" type vehicle, is characterized by a long slender aerodynamic body, and control surfaces are utilized for maneuvering forces. The Wood's Hole Oceanographic Institute's (WHOI) REMUS is a good example of a torpedo type vehicle. This type of vehicle is very efficient at traveling long distances at high speeds. However, at low speeds, the control surfaces provide no maneuvering forces and the vehicle cannot accurately control its trajectory. The second class of vehicles is termed a "box" design. This type of vehicle is characterized by a bulky shape (low aspect ratio), with multiple thrusters positioned at several locations to provide the necessary control forces in any direction. These vehicles offer much more accurate low-speed maneuvering but have very low top speeds and low efficiency for long-range transit. Remotely operated vehicles (ROVs) rely on a tether for power and control, which inherently limits mobility. Hence, the majority of ROVs utilize a box design like WHOI's Jason or Monterey Bay Aquarium Research Institute's (MBARI) Ventana. Additionally, traditional propeller-type thrusters are very efficient when operating at nominal rotation rates. However, accurate positioning often requires short impulses, which correspond to propeller rotations on the order of single rotations that result in unpredictable control forces [2]. This coupled with the unpredictability of the environment causes traditional propeller-type thrusters to be nonideal for accurate maneuvers.

Vehicles have been designed that utilize tunnel thrusters, which run through the hull of the vehicle to give low-speed maneuver capabilities to vehicles without compromising the forward drag profile. However, tunnel thrusters have been determined to be less effective when a cross-flow is present and have been observed to continue producing a force, even after being terminated [3].

One of the most desirable components of autonomous underwater robots is an ability to provide continuous on-demand observation and data collection. This could be in the form of environmental monitoring (temperature, salinity, and ocean current velocity measurements) or more active sensing networks, like coastal-traffic monitoring. Vehicles, which are meant to be included in an autonomous ocean-sampling network (AOSN), [4]–[6] must have the capabilities of both torpedo- and box-type vehicles. Because a completely autonomous sensor-network vehicle must have some means of refueling, compiling data, and receiving new mission objectives while still maintaining a rapid travel time and long-range endurance so that the vehicle's characteristic survey time is below the cycling time associated with the study dynamics [7].

Biological motivation: One marine species, which demonstrates an ability to travel long distances during migration [8],

Manuscript received December 23, 2009; revised March 9, 2010. This paper was recommended for publication by Associate Editor C. C. Cheah and Editor W. K. Chung upon evaluation of the reviewers' comments. This work was supported in part by the Office of Naval Research under Project 1545312 and in part by the National Science Foundation under Project 1546041.

The authors are with the Aerospace Engineering Sciences, University of Colorado at Boulder, Boulder, CO 80309 USA (e-mail: Mohseni@colorado.edu).

This paper has supplementary downloadable material available at htttp://ieeexplore.ieee.org. provided by the author. The material includes one video. The size is not specified. Contact mohseni@colorado.edu for further questions about this work.

Color versions of one or more of the figures in this paper are available online at http://ieeexplore.ieee.org.

Digital Object Identifier 10.1109/TRO.2010.2046069

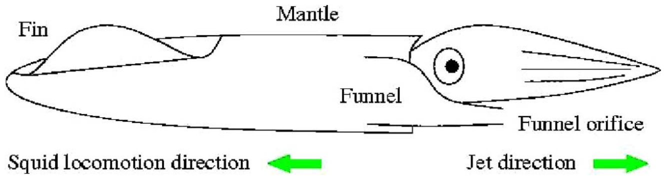

Fig. 1. Conceptual diagram of underwater-jet locomotion.

as well as accurate small-scale maneuvers (which is seen in their success as predators [9], [10]) is the squid. To propel itself forward, a squid first ingests surrounding fluid into its mantle cavity through a slit behind the head. After the fluid has been fully absorbed, the head is pulled back toward the body closing off the intake vents. A series of ring muscles circumscribing the mantle are then contracted forcing the fluid through a nozzle called the siphon located under the head near the tentacles. The high-energy shear layer rolls into a vortex ring, which carries the high-momentum fluid jet far from the squid, as is illustrated in Fig. 1. This method of underwater-jet propulsion has been largely overlooked by the maritime community, and thus, little is known about the actual mechanisms for creating thrust. Our group, in an effort to understand these basic dynamics, developed both computational and mechanical tools to study this method of thrust production. The exact methods of thrust production and fluid transport in various species of jellyfish were studied computationally in [11]–[13]. Additionally, we developed a mechanical analog: a thruster, which creates a jet similar to a squid to determine important operational parameters for generating thrust. This new kind of thruster may prove to be an ideal solution in autonomous sensor-network applications. For reference, a computer-aided design (CAD) model of the thruster prototype (designed to independently control operational parameters) is shown in Fig. 2, and a final version of the actuator designed to operate at optimal conditions is shown in Fig. 3. The actuator itself is contained entirely within the vehicle with only a small opening at the surface of the vehicle. Therefore, these control devices have a minimal impact on the forward-drag profile of the vehicle, allowing for efficient long-range travel. Additionally, the placement of these actuators allows for complete thrust vectoring, even when the vehicle has zero forward velocity. This allows for a complete range of motion for docking purposes.

This paper will describe the important considerations, which are essential toward implementation of this type of thruster in an underwater-robot architecture and will be organized in the following manner. Section II will describe the basic concept of the actuator. Section III will describe the testing setup and summarize the results determined from static testing. The time-dependent response of the thruster will be discussed in Section IV. Typical vehicle architecture and thruster implementation will be analyzed in Section V. Section VI will analyze the actual frequency response of the thruster vehicle system (both open- and closed-loop response). Section VII gives a description of a disturbance rejection algorithm which can be utilized in marine environments. A summary of the future direction of research and work, which still needs to be done on this technology, is given in Section VIII. Concluding remarks are presented in Section IX.

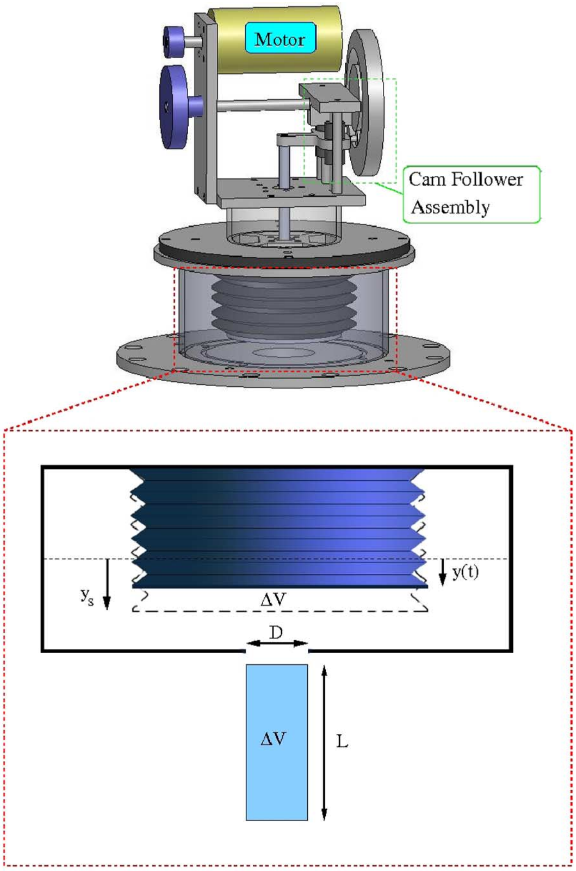

Fig. 2. CAD model of the adjustable experimental thruster with a conceptual model of the fluid-manipulator section.

II. THRUSTER DESCRIPTION

The first tests were performed on a prototype of the vortex-ring thruster (VRT), which was designed to be easily adjustable rather than compact. A CAD model of this prototype is depicted in Fig. 2 as well as a conceptual diagram of the critical components, which affect the thrust generation. The thruster can be thought of in similar terms to the squid example; the device consists of a large cavity (internal to the vehicle) similar to the squid mantle, with a fluid manipulator inside of it, which changes the volume of the cavity and forces fluid in and out of an opening at one end. By successive ingestion and expulsion of fluid, the thruster creates an array of high-momentum vortex rings, which impart their impulse on the vehicle. The fluid manipulator used in this experiment is a semiflexible accordion-style bellows. This plunger is reinforced to ensure consistent fluid-volume flux with respect to linear deflection of the plunger. Even though the device has zero net-mass flux (since the ingestion and expulsion phases move the same amount of fluid through the single orifice), it has a positive momentum flux similar to synthetic-jet devices used in air for flow control; for more information on synthetic jets, see the review by Glezer and Amitay [14].

Experimental thruster: The thruster in this investigation utilizes a mechanical-driving mechanism to ensure consistency and provide independent control of operational parameters; however, studies have also been performed using thrusters

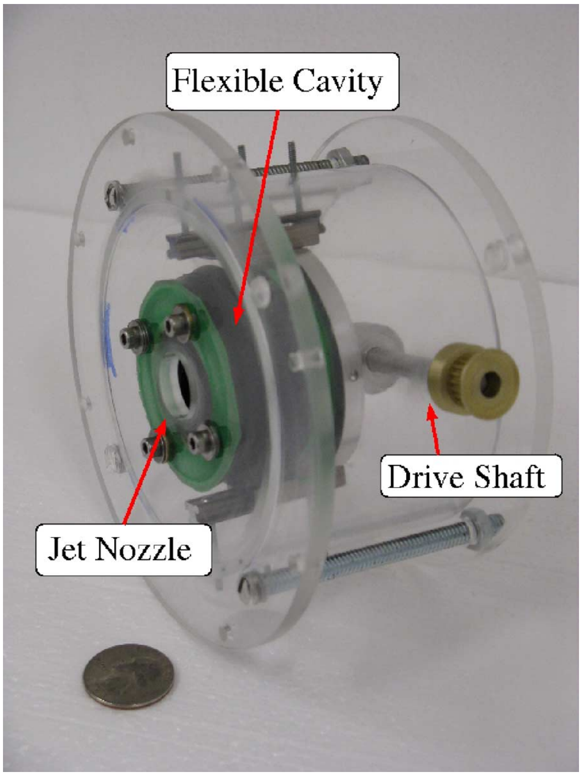

Fig. 3. Vehicle model VRT in transparent housing to allow visual access to components.

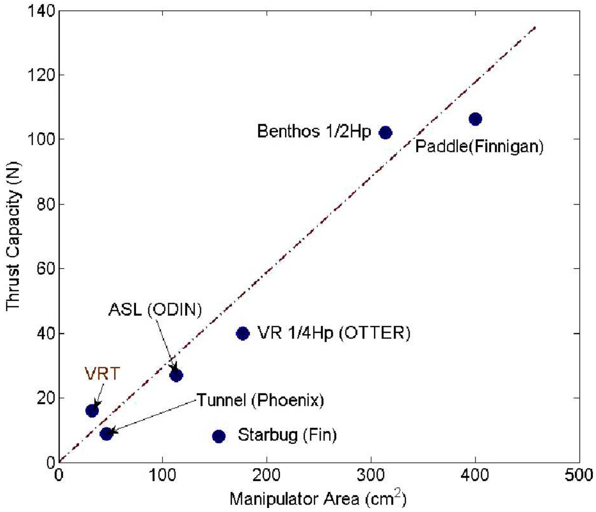

Fig. 4. Comparison of fluid-manipulator geometry with thrust capacity for a range of thrusters found on different 6-DOF vehicles.

with solenoid drivers [15] as well as acoustic actuation [16]. The mechanical-driving mechanism consists of a feedback-controlled dc motor geared down to increase torque, connected to a disk cam, whose track drives the linear motion of the fluid manipulator. The cam used in this investigation creates a sinusoidal-plunger deflection when a constant rotational velocity is applied to it. The driving mechanics are further discussed in Section IV-B.

Fig. 3 shows a later model of the thruster, which was installed in a test vehicle (this vehicle is discussed specifically in Section VIII and is shown in Fig. 18). This version of the thruster clearly demonstrates the compact modular aspect of these thrusters. In fact, the volumetric impact of the thruster on the vehicle is very similar to that of a typical propeller-type thruster. Fig. 4 shows the relationship between peak-thrust output and fluid-manipulator area for various maneuvering thrusters found on vehicles with 6 degrees-of-freedom (DOF) capabilities. The efficiency of motors and other drive mechanisms is independent of the method of fluid actuation used to generate thrust. Therefore, different thrusting technologies should be compared on the basis of the fundamental manipulator used to drive the fluid. For propellers, this manipulator is the propeller blade itself, whereas the VRT of this investigation uses a flexible plunger within the internal cavity so that the manipulator area is the surface area of the plunger face. This comparison contains several other experimental thrusters designed to give vehicles accurate maneuver without compromising the forward drag, including tunnel thrusters installed in the Phoenix autonomous underwater vehicle (AUV) [17], low-profile propeller thrusters located within the control surfaces of the Starbug AUV [18], and paddling fins (which can be used as control surfaces at high forward velocities) like those found on Finnigan the Roboturtle [19], [20]. Additionally, the comparison includes commercially available externally mounted propeller thrusters (typical of box-style vehicles), including the benthos 1/2-Hp model thruster found on the MiniRover and Stingray [21], [22], the 1/4-Hp variable reluctance thrusters found on MBARI's OTTER (also a hybrid-class vehicle) [23], and ASL thrusters used on ODIN (an experimental high-accuracy vehicle) [24]. The thrust capacity and manipulator area presented in this comparison for the VRT are based on the vehicle-thruster model of Fig. 3. It should be noted that the majority of propeller thrusters have the same ratio of thrust capacity to manipulator area (this is shown by the dotted line), including the tunnel thrusters. The slight variations from this general curve are because of changes in blade angle to increase directional efficiency. The exception being the low-profile propeller thruster, which is limited by the fact that the driving mechanism is integrated into the propeller itself significantly decreasing the total volumetric impact on the vehicle. It can be seen that the VRT is volumetrically competitive with propeller-type thrusters, which means that for a given design thrust capacity, using VRTs will not take up any more volume than a commercially available propeller thruster. However, using a VRT will eliminate the need for complicated piping (like tunnel thrusters), decrease time for the thrust to settle (see Section IV), and improve small-scale impulsive thrust accuracy. Since, this is still a very new technique for generating thrust, at this stage our effort has focused on hydrodynamic and mechanical characterization of the thruster. Therefore, the power consumption has not been extensively characterized; however, as a general point of reference, the thruster of Fig. 4 operating at maximum capacity consumes on the order of 12 W.

Fig. 5. Thruster-testing tank developed for this experiment. The tank is approximately 1 m × 1.3 m × 2.3 m.

III. Static Thruster Testing

A. Experimental Setup

The thruster described in Section II was suspended in a fluid reservoir contained in a 2.5-kL testing tank (designed specifically for this investigation), which is shown in Fig. 5. A bearing arrangement connected to the frame of the tank is located at the top and restricts the motion of the thruster canister to a single axis. The thrust generated in this direction was measured using a PCB 1102 load cell and was sampled at 10 kHz.

B. Summarized Results

The VRT was operated over an entire range of operating conditions in [25] and [26] to determine the dependence of thrust production on the characteristic operational parameters. A model was developed to predict the thrust output of the VRT. This model assumed that the expelled jet is contained within a single, distinct slug of fluid. The rates of change of impulse, circulation, and energy of this fluid slug were assumed to be identical to the flux of those quantities across the opening of the thruster. This slug model predicted the thrust with respect to the momentum flux across the opening of the device. It was assumed that the fluid exits the thruster with a uniform velocity and that there is no net momentum flux during the ingestion phase, since the fluid starts and ends at rest (for a more in-depth description of the slug model, see [25]). This model predicts that the thrust would be dependent upon the thruster-pulsation frequency as well as the geometric constraints on the fluid jet. More specifically, if the jets are pulsed with a sinusoidal exit velocity profile, the average thrust (over an entire pulsation cycle) is given by

$$\bar{T}_{\mathrm{ss}} = \rho \frac{\pi^3}{16} L^2 D^2 f^2. \tag{1}$$

In this equation, f is the thruster-actuation frequency, ρ is the fluid density, $\bar{T}_{\mathrm{ss}}$ is the mean steady-state thrust, and L and D are the length and diameter of a hypothetical cylinder of fluid (see Fig. 2), which would be the same size as the fluid jet, if no shear effects were present. For these jets, the diameter will be considered the characteristic geometry. The length of the jet scaled by the diameter (L/D) is known as the stroke ratio. In some studies [27], [28], this ratio is referred to as the "formation time," since it is also equal to the time since the jet was first initiated, nondimensionalized by the jet velocity and diameter $L/D = \int_0^{t_e} U_j dt/D$, where t_e is the expulsion time (time required for the jet to be ejected).

It is observed that for higher stroke ratios, the thrust saturates after a critical frequency is reached. This critical frequency decreases as the stroke ratio is increased. This phenomenon is attributed to the vortex ring pinch-off or separation from trailing shear flow and is explained in [25], which contains an in-depth analysis of the effect that different jetting parameters have on thrust production. For the investigation of this paper, the stroke ratio was set to a constant value of approximately 5. This value of the stroke ratio was chosen so that (for a given jet volume) the thruster will produce a maximum thrust without experiencing pinch-off. This allows the thrust to be accurately modeled by (1).

IV. Transient-Thruster Response

The static testing from previous experiments summarized in Section III verified the validity of the slug model in predicting the average thrust produced at various operating conditions; however, it tells nothing about the transient behavior of the thruster. In fact, the thrust produced is a highly dynamic one. The complete description of these transient characteristics is necessary for the implementation of any high-accuracy control algorithm.

There are two major characteristics of the thruster's transient behavior, which were observed during the experimentation in this paper. The first feature is a settling time associated with reaching the average thrust defined by the slug model. Similar to propeller-type thrusters [2], [29], the VRT has time delays, which are inversely proportional to the desired level of thrust. However, it should be noted that this type of thruster has settling times on the order of fractions of a second, whereas typical propeller-type thrusters experience settling times on the order of several seconds [2], [29]. This settling time can be modeled in similar terms to a first-order linear damper $d\bar{T}/dt = \left(\bar{T}_{\mathrm{ss}} - \bar{T}\right)(1/\tau)$. In this expression, $\bar{T}_{\mathrm{ss}}$ is the steady-state level of thrust described by (1), which is purely a function

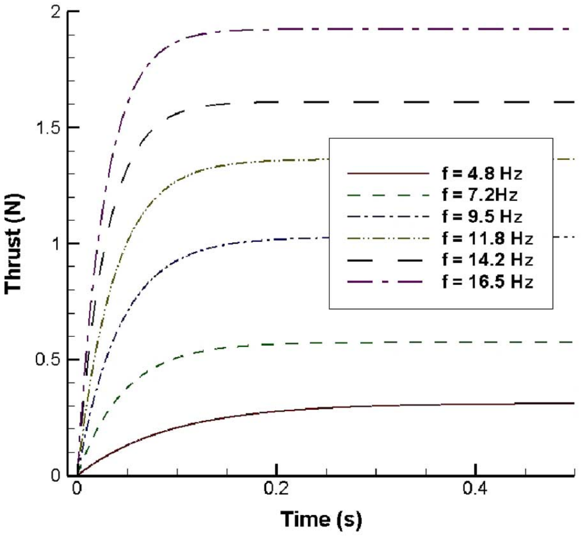

Fig. 6. Thruster transient response fitted to a first-order delay.

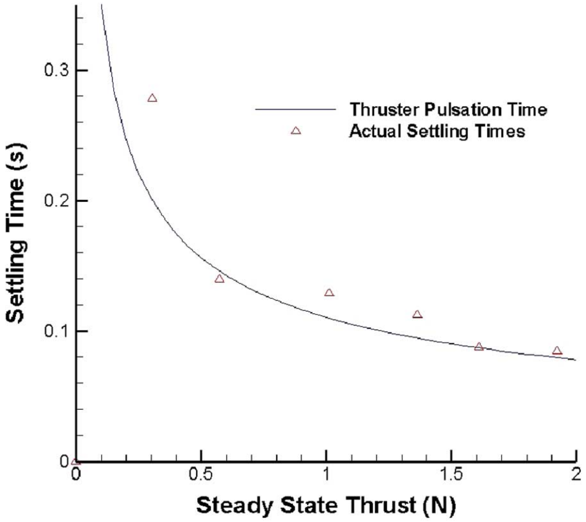

Fig. 7. Thrust-settling time as a function of steady-state thrust level.

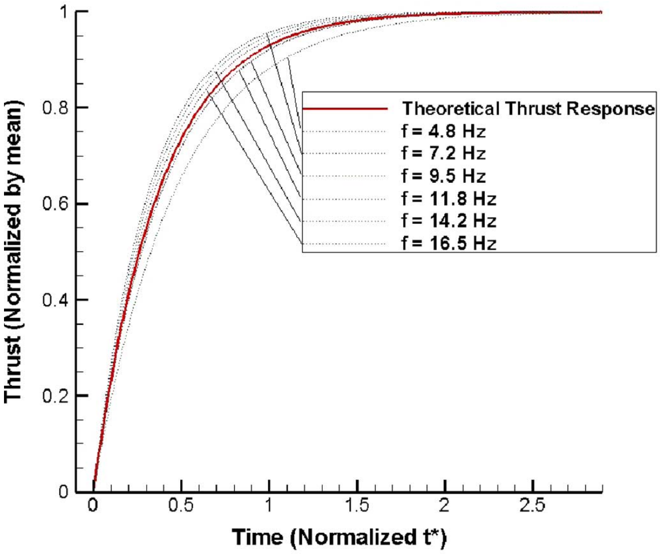

Fig. 8. Normalized thrust $\bar{T}^\star$ versus normalized time for all cases of steady-state thrust $\bar{T}_{\text{ss}}$. Actual thrust values shown with dotted lines and theoretical curve based on average time constant shown in solid red.

of the driving parameters (and can, therefore, be thought of as a control signal), $\bar{T}$ is the dc component of the transient-thrust signal, and τ is a time constant, which is a function of $\bar{T}_{\text{ss}}$. Assuming that the thruster starts at rest and that the steady-state thrust is held constant, the solution of the thrust equation becomes

$$\bar{T}(t) = \bar{T}_{\text{ss}}\left(1 - e^{-t/\tau}\right). \tag{2}$$

Several time-dependent thrust datasets were analyzed to determine the settling time dependence on steady thrust level. Using a least-square approximation, the transient thrust sets were fit to the form given previously to determine the damping time constant τ for each set. The dynamic thrust curve for several steady state thrust levels fitted to a first order damper are given in Fig. 6. The settling time can be determined from these fitted curves as the time, where the thrust reaches 95% of the steady state thrust, which corresponds to three time constants after the thruster had been activated. A characteristic time scale for the thruster, which can be determined from the steady state thrust is the period of a single pulsation, since it is inversely proportional to the square of the steady state thrust level (1). Fig. 7 demonstrates that the thruster tracking period provides a good characteristic time constant for describing the thruster tracking dynamics, since the actuation period is almost identical to the time delay calculated from the fitted curves.

Although the rise time is dependent on the level of thrust, the strong correlation between settling time and actuation period suggest that it should be possible to converge upon a single nondimensional time constant, which is scaled by the oscillation period. Consider the nondimensional equation

$$\bar{T}^\star(t^\star) = 1 - e^{-t^\star/\tau^\star} \tag{3}$$

where $\bar{T}^\star = \bar{T}/\bar{T}_{\text{ss}}$ is the thrust normalized by the steady-state thrust, and the time is normalized as $t^\star = tf$ with characteristic time $1/f$ equal to the actuation period. The datasets shown in Fig. 6 were all normalized to the new variables $\bar{T}^\star$ and $t^\star$. The set of normalized curves is shown in Fig. 8. This graph clearly shows that normalizing the thrust by the steady state value and the time by the oscillation period results in self-similar behavior of the thrust. The theoretical normalized thrust curve, where $\tau^\star = 0.38$, which is the average of all the datasets, is depicted as a solid line. The actual normalized datasets are shown by the dotted lines. The actual distribution of the term $\tau^\star$ for each dataset is presented in Fig. 9.

It should be seen from Fig. 9 that the actual time constants of the normalized sets are well approximated by the mean value, which is used for the theoretical curve. In general, these time constants are located about the mean with a random variance, which increases in magnitude as the steady state thrust level decreases. This general error trend is indicative of the nature of the thruster, as well as the measurement setup. As the mean thrust

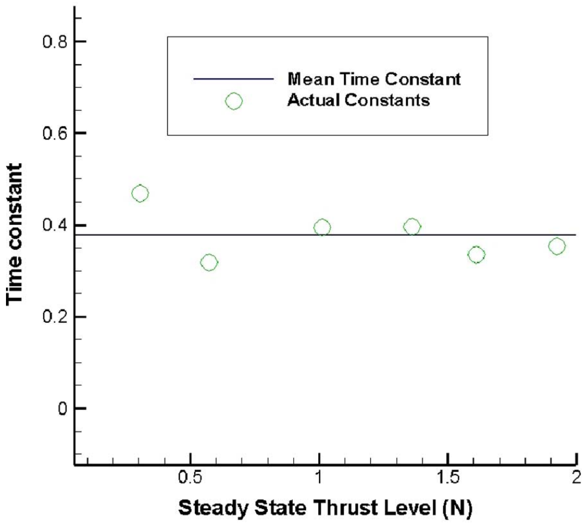

Fig. 9. Time constants calculated by least-squares approximation to fit normalized data sets to the form of (3).

level decreases, the random electrical and structural noise stay at the same level so that the data at the low thrust ranges is much more sensitive to random noise. Additionally, the actuation period increases significantly as the thrust level decreases, which means that sensor drift associated with our load cell has a longer time to affect the thrust data in the low-thrust range, which further exaggerates the general error trend.

The second feature of the transient thruster response (which remains undamped throughout actuation) is a sinusoidal-wave mode associated with the pulsation of the actuator. When these two modes are incorporated into the thrust model, it takes on the following form:

$$T(t,f) = \bar{T}_{\text{ss}}\left(1 - e^{-tf/\tau^\star}\right) + a\sin(2\pi f t) \tag{4}$$

where f is the pulsation frequency of the thruster, and a is the amplitude of oscillation associated with the pulsation, which can be determined from the slug model along with the steady state thrust. The slug model predicts that the amplitude a is proportional to the square of the actuation frequency so that the ratio $a/\bar{T}_{\text{ss}}$ is a constant for all driving frequencies. This ratio will be denoted η and can be considered a representation of a dynamic thruster efficiency (ratio of the thrust oscillation amplitude to the dc offset). For a thruster with a sinusoidal jet-velocity profile, like the one used in this experiment, this ratio has a value of $\eta = 4$. Taking this relation into account and incorporating the steady state thrust, (1), gives an equation for the thrust as a function of time and actuation frequency

$$T(t,f) = C_v f^2 \left[\left(1 - e^{-tf/\tau^\star}\right) + \eta\sin(2\pi f t)\right] \tag{5}$$

with $C_v = \rho(\pi^3/16)L^2 D^2$ being a thruster constant describing the operating parameters of the thruster (since D and L are fixed during operation).

A. *Spectral Modeling*

Invariably, a high-accuracy maneuvering system will be required to operate in chaotic environments. The energy of these turbulent marine environments is well defined in the spectral domain [30]. A linear time-invariant (LTI) transfer function model of the thruster dynamics is desirable, since it allows the thruster parameters to be selected with respect to the mission specific environmental dynamics. Additionally, this model could be used within a relative fluid velocity estimator scheme to compensate for fluid disturbances as discussed in Section VII.

If the thrust (5) is mapped into the spectral domain through a Laplace transform, it becomes a nonlinear integral function of the frequency input

$$\begin{aligned} \hat{T}(s) &= C_v \int_0^\infty f^2 H(f,s)dt \\ H(f,s) &= e^{-st} - e^{-t(s+f/\tau^\star)} \\ &\quad + \frac{\eta}{2i}\left[e^{-t(s-2\pi f i)} - e^{-t(s+2\pi f i)}\right] \end{aligned} \tag{6}$$

which can be linearized by setting the input function, which in this case is the frequency, equal to a weighted Heaviside function $f(t) = f_0 \int_0^t \delta(\tau)d\tau$ scaled by some nominal pulsation frequency f_0. The linearized equation is as follows:

$$\hat{T}(f,s) \approx C_v\left(\frac{f_0^2}{s} - \frac{f_0^2}{s + f_0/\tau^\star} + \frac{\eta 2\pi f_0^3}{s^2 + 4\pi^2 f_0^2}\right). \tag{7}$$

The transfer-function plant for the thruster is, therefore, the ratio $\hat{T}(s)/F(s)$, where $F(s)$ is the Laplace transform of the input function $F(s) = \int_0^\infty f(t)dt = f_0/s$. Using this relation, the thruster plant can be determined. This should be an accurate approximation so long as the rate of change of $f(t)$ is slow with respect to vehicle dynamics

$$G_{\text{VRT}}(s) = C_v\left(\frac{f_0^2}{\tau^\star s + f_0} + \frac{\eta 2\pi f_0^2 s}{s^2 + 4\pi^2 f_0^2}\right). \tag{8}$$

Therefore, the thruster plant describes the linearized dynamics between the input actuation frequency and output thrust and is purely a function of the trim frequency f_0.

B. *Thruster Driving Mechanism*

It should also be noted that the fluid manipulator within the thruster could be driven with a variety of actuators and that the choice of driving mechanism will have no effect on the thrust production, so long as the driving frequency is accurately maintained. In our experimentation, this frequency is controlled independently through the use of an electric motor and AMC motor controller. The loop gain of the motor controller was set high enough so that the motor dynamics could be ignored, and a voltage input to the motor controller is directly proportional to the motor frequency, as well as the actuation frequency. Similar methods could be performed for any actuator used to drive the manipulator. Therefore, the system model predicts that $f(t)$ will be proportional to the input voltage. This trend was determined empirically so that the contributions of the motor/controller system could be modeled by a single gain term K_{MC}, which relates input voltage to thruster-driving frequency.

V. VEHICLE MODELING AND THRUSTER IMPLEMENTATION

Consider a simple underwater vehicle to be modeled by a cylinder in a fluid with a single DOF. The governing equation for the system is given by the simple drag equation

$$M\ddot{x} = T - C_d \dot{x}_r |\dot{x}_r| \tag{9}$$

where x is the unrestrained axis, M is the mass of the vehicle (including an added mass), T is the instantaneous force provided by the thruster, $\dot{x_r}$ is the relative vehicle velocity $\dot{x_r} = \dot{x} + u_{\rm fluid}$, C_d is a drag coefficient defined by $C_d = 1/2\rho S C_D(Re)$, S is the wetted area of the vehicle, and $C_D(Re)$ is the coefficient of drag of a cylinder in a laminar cross flow, which is a fair assumption, since the primary uses of these thrusters are for maneuvers involving rotation and sideways translation at low speeds, both of which induce a laminar cylinder cross flow. Without loss of generality, the relative velocity will be considered equal to the inertial velocity (i.e., $u_{\rm fluid} = 0$). If the nonlinear-drag term is linearized about some nominal trim velocity $\dot{x}_{\rm trim}$, then the governing equation of the vehicle can be modeled by a plant in the spectral domain with the following form:

$$G_{\rm sub}(s) = \frac{1}{ms^2 + Cs} \text{ and } C = \frac{1}{2}\rho S C_D(Re)\dot{x}_{\rm trim} \tag{10}$$

where the input is the transient thrust of the thruster, and the output is the position of the vehicle along the x-axis.

A. *Maneuver Scaling and Trim Conditions*

The ultimate goal of this type of maneuvering technology is to achieve a high-accuracy loiter or hover so that the vehicle can engage some docking mechanism and perform autonomous upkeep. Marine environments are cluttered with wave like current disturbances. To overcome these disturbances, a vehicle must provide a wide range of controlling forces. It becomes apparent that the performance of a controller in this type of an environment can be most usefully characterized by a frequency analysis, whereby the inputs to the system are sinusoidal maneuvers of the form

$$x_d = A\sin(\omega t) \tag{11}$$

with x_d being the desired vehicle position, A is the maneuver amplitude, and ω is the maneuver frequency.

It should be noted that the model developed for the thruster-vehicle system was derived using several approximations and linearizations. The actual dynamics of the system are highly nonlinear so that the choice of design points to linearize about has a strong effect on the predicted dynamics of the system. Therefore, the selection of these design points deserves careful consideration. Typically, these parameters would be defined in terms of actual vehicle requirements, but we would like to extend a more general analysis. That is, to define optimal vehicle parameters with respect to maneuver capabilities and maneuver parameters.

Consider again that the drag model assumes the vehicle to be a perfect cylinder in cross flow. The characteristic size of a cylinder in this flow is the diameter. If all vehicles are assumed to have the same aspect ratio (which we will denote σ), then the geometry is reduced to the diameter d. The relative size of a maneuver plays a large role in determining the dynamics of the vehicle performing that maneuver. This quality can be characterized by the ratio of maneuver amplitude to the vehicle-characteristic length $A^\star = A/d$, which will be referred to as the scale factor of the maneuver. If we characterize according to scale factors, then maneuvers can be thought of as members of three regimes. Maneuvers in the *Cruising regime* are characterized by maneuvers that are much larger than the vehicle size, and maneuvers in the *Docking regime* are characterized by maneuvers that are much smaller than the vehicle size. Maneuvers with amplitudes on the same order as the vehicle size are in the *Transition regime*, which is required to transition between the *cruising* and *docking* modes.

B. *Scaling the Problem for Unitary Amplitude*

This section describes a method for scaling the vehicle-control problem so that maneuvers in different regimes can be analyzed using consistent nomenclature as in the frequency response analysis described in Section IV-A. It is convenient from a frequency analysis point of view to scale the problem so that the maneuver amplitude attains unity ($A = 1$). Through this mapping, a maneuver with a smaller amplitude may be modeled by a larger vehicle with unitary amplitude. The geometric scale is fairly straightforward. The vehicle diameter can be recast as $d = 1/A^\star$, and assuming that the vehicle is designed to approach neutral buoyancy, then the mass of the vehicle becomes $M = \rho\pi/A^{\star 3}$. In order to maintain consistency, the thruster response must be scaled appropriately to incorporate the larger vehicle. The limitation on the thruster is the maximum thrust it can produce while still being accurately described by the slug model, which, in the vehicle model, shows up as a maximum voltage that can be applied to the motor controller $V_{\max}$. If a thruster bounded by maximum thrust $C_v\,(V_{\max} K_{MC})^2$ is operating on a vehicle of mass $M(A^\star)$, the maximum acceleration it can attain can be derived from Newton's second law (assuming the vehicle is at rest and being forced with the maximum thrust). This maximum acceleration will be considered the design criterion for vehicle-thruster selection. Consider a thruster (characterized by K_{MC_0}), which is selected for a vehicle of characteristic size d_0. The criterion on the thrust capacity requires that the system's maximum acceleration is equal to the maximum-required maneuvering acceleration (given $A^\star = 1$). Some algebra gives a natural maneuver frequency, where this design constraint holds true:

$$\omega_0 = \left(\frac{C_v}{\rho\pi}\right)^{1/4} \left(\frac{K_{MC_0} V_m ax}{\omega_0}\right)^{1/2}. \tag{12}$$

Additionally, as the maneuver regime changes, the maximum acceleration required by the desired maneuver increases proportionally to the scale factor ($\ddot{x}_{d,\max} = A^\star \ddot{x}_{\max}$). This is the condition that will be enforced to ensure a consistent thruster scaling.

Now consider the scaled vehicle, which ensures unitary amplitude, whose diameter and mass are purely a function of the scale factor. The maximum acceleration of this vehicle can similarly be defined in terms of the scaled unknown thruster gain $K_{MC}(A^\star)$. Furthermore, the maximum acceleration of the desired maneuver will always be the square of the maneuver frequency (since it has unitary amplitude). If the maneuver frequency is set equal to the natural maneuver frequency of the actual thruster-vehicle system, and the relation between accelerations is enforced, then the scaled thruster gain can be solved as a function of the natural vehicle parameters and the scale factor

$$K_{MC}(A^\star) = K_{MC_0}\frac{1}{A^{\star 2} d_0^2}. \tag{13}$$

If we define a natural scale factor for the system as $A_0^\star = 1/d_0$, then the equation for the scaled motor gain takes on a much more esthetic form given by

$$K_{MC}(A^\star) = K_{MC_0}\left(\frac{A_0^\star}{A^\star}\right)^2. \tag{14}$$

Similarly, the trim velocity used in drag linearization can be rescaled in terms of the maneuver regime parameter, which results in a new coefficient term in the vehicle model (10)

$$C = \frac{K_{MC}V_{\text{trim}}}{A^\star}\sqrt{\frac{\rho C_D C_v \sigma}{2}} \tag{15}$$

where V_{trim} is a trim voltage, which should be somewhere in the middle of the range of possible controller signal voltages correlating to the voltage required to attain the trim velocity. Therefore, a maneuver defined by a given scale factor being performed by a vehicle with specific parameters can be similarly analyzed by a unitary maneuver being performed by a scaled-equivalent vehicle, whose thruster strength is characterized by (14) and whose drag is characterized by (15).

VI. HYBRID SIMULATION

Because of the abundance of complexities involved with the control of a fully unrestrained vehicle, a simpler method is desired to determine the actual dynamic performance of a thruster. A method is used whereby the behavior of a vehicle is modeled as a virtual vehicle, and the thrust is measured empirically from a thruster in a controlled static setup. Using this procedure, the validity of the thruster model, as well as the linear vehicle drag approximations, can be tested with respect to a "pure" vehicle, which acts predictably according to the fully nonlinear drag equations. In addition, approximation/modeling errors may be determined independently from inconsistencies because of environment unpredictability. The virtual vehicle will be fully described by the drag equation given by (9). In this case, the thrust term T will be the actual thrust measured directly from the VRT, within the setup depicted in Fig. 5.

The virtual vehicle model assumes that the vehicle starts at rest. At the onset of the experiment, the vehicle is given some form of driving signal from a vehicle controller. The corresponding force from the thruster is measured directly using a load cell. The thrust is then fed into the virtual algorithm, and the vehicle motion is integrated according to (9). In real time, the control algorithm drives the virtual vehicle using the actual forces generated by the thruster within its test environment. A functional block diagram of this system is shown in Fig. 10.

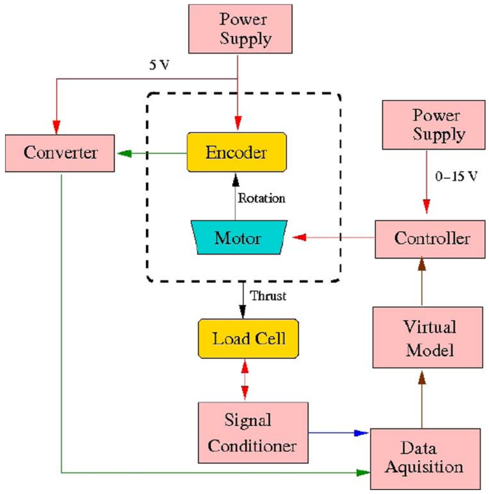

Fig. 10. Testing setup and hybrid-simulation functional-block diagram.

Of course, this simple drag model ignores many of the key parameters, which would affect the operation of an actual vehicle with this type of thruster; most notably, the effect the surrounding flow will have on the thrusters. It was determined by Krueger *et. al.* [31] that jets produced in the presence of a background coflow will experience "pinch-off" at a lower stroke ratio, as the flow velocity approaches the jet velocity. Since a moving vehicle will experience a cross flow (which corresponds to a thruster coflow) the effects of coflow on thrust should not be dismissed, but are difficult to model in a virtual environment. In spite of the simplicity of the model, it allows for the performance of the thruster to be observed much more easily, without the arduous process of performing tests with an actual vehicle.

A. *Frequency Response*

Within the hybrid simulation, the open-loop frequency response was determined for the thruster-vehicle system. This response was tested (over a maneuver frequency range encompassing the –3 dB cutoff frequency) for three different maneuver scale factors; $A^\star = 3$, which represents the *Cruising regime*, $A^\star = 1$ to characterize the *Transition regime*, and $A^\star = 0.5$ for the *Docking regime*. As an example, the open-loop frequency response of the system in the *Cruising regime* is shown in Fig. 11. As can be seen from this figure, the spectral model is an appropriate representation of the frequency response. It should be noted here that the modeled response was calculated assuming a pulsation frequency sufficiently higher than the maneuver frequencies. For this particular regime, the model assumes a thruster frequency of $f_0 = 20$ Hz; however, the thruster trim frequency could be set significantly lower for the other regimes and still maintain accuracy, because of the lower thrust requirements in general, for those regimes. Additionally, it should be noted here that the hybrid simulation adjusted the amplitude of the maneuver to bring it into the *Cruising regime*, which is how the experimental data was determined. By contrast, the

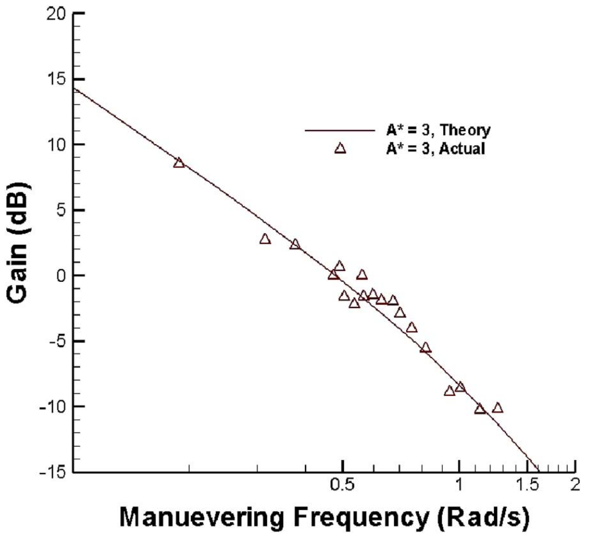

Fig. 11. Open-loop frequency response for the thruster-vehicle system in the *Cruising regime* ($A^{\star} = 3$).

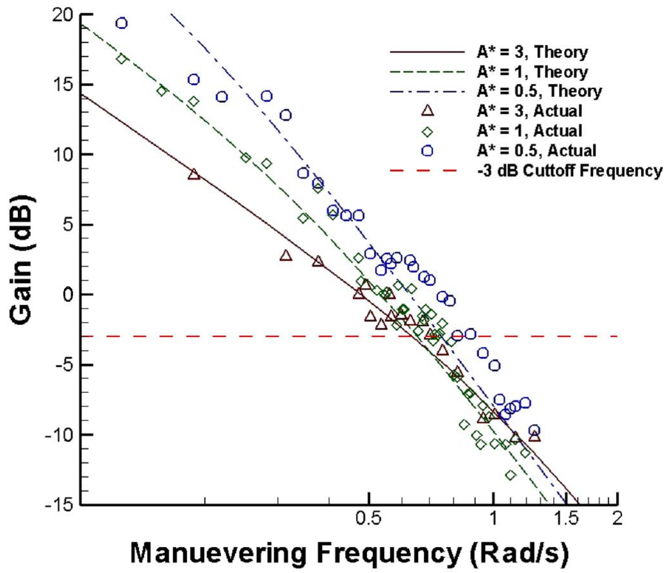

Fig. 12. Open-loop frequency response for the thruster-vehicle system. *Cruising regime* shown by $A^{\star} = 3$, *Transition regime* shown by $A^{\star} = 1$, and *Docking regime* shown by $A^{\star} = 0.5$. Theoretical response modeled assuming $f_0 = 20$, 9, and 5 Hz, respectively.

theoretical frequency response curve was modeled in the scaled space with unitary amplitude described in Section V-B. Therefore, this frequency trend not only demonstrates the accuracy of the linearized spectral model but also the accuracy of the maneuver scaling procedure as well.

The response curves for all three regimes along with those predicted by the transfer function model (assuming pulsation frequencies of 20, 9, and 5 Hz, respectively) are shown in Fig. 12. It can be seen from this graph that the constant pulsation frequency approximation accurately models several features of the frequency response, including the cutoff frequency and the convergence of different maneuver regime response curves near the cutoff frequency. Another interesting feature is located in the low frequency maneuvers. Here, the spread between the maneuver regimes is more drastic than at the corner frequency of the system (which happens to be nearly identical for all three maneuver regimes). This is indicative of the fact that at low maneuver frequencies, the thruster is required to deliver smaller forces, which, in turn, result in lower actuation frequencies, so that at this level, the vehicle experiences individual pulsations. In the low-amplitude *Docking regime*, this results in a higher gain, since pulsations enact an acceleration before drag forces take effect. In the *Cruising regime*, however, this results in less gain, since the drag terms dominate between pulsations. This trend is accurately captured by the model. Although the simulation was not run for higher maneuver frequencies, the model predicts that the vehicle in the *Cruising regime* will achieve a higher amplitude maneuver in the high frequency ranges, which is suggested by the slopes of the experimental trends.

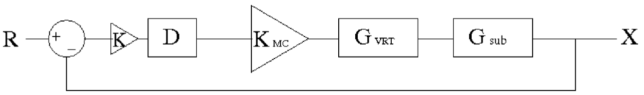

Fig. 13. Feedback loop for the thruster-vehicle system.

B. Feedback Control

Now that we have approximated all necessary transfer functions, a feedback controller for the system can be analyzed. Consider the feedback loop shown in Fig. 13 for all maneuver regimes, where $D(s)$ is the controller compensation. The vehicle-position error is easily found by $\tilde{x} = x_d - x$, where x_d is the desired maneuver trajectory described by (11), and x is the vehicle position as calculated from (9). Assuming a simple proportional-derivative (PD) feedback system, the controller compensation can be described in spectral space by

$$D(s) = K(T_D s + 1) \tag{16}$$

where K is the feedback gain, and T_D is a characteristic timing term associated with the derivative gain. The closed-loop frequency response of the system under PD control is depicted in Fig. 14. The important parameters, which drive the controller gain selection are motivated by different goals for the different maneuvering regimes. The *Docking Regime* requires very accurate tracking with minimal overshoot, whereas the *Cruising Regime* is generally indifferent to overshoot and is much more concerned with a fast approach time (so that the vehicle can move to a site of interest before the phenomena of interest dissipates). For this study, the feedback gain was set to 4, which was chosen to keep the required thrust within the thruster capacity, and T_D was set to 0.75 to keep the position overshoot within acceptable bounds in the *Docking regime*.

The system closed-loop frequency response was determined over a similar frequency range for the same maneuver scale factors as the open-loop response. The pulsation frequency f_0 for the linear model was set to the same driving frequencies as the open-loop case. This model is seen to approximate the closed-loop behavior of the thruster-vehicle system sufficiently,

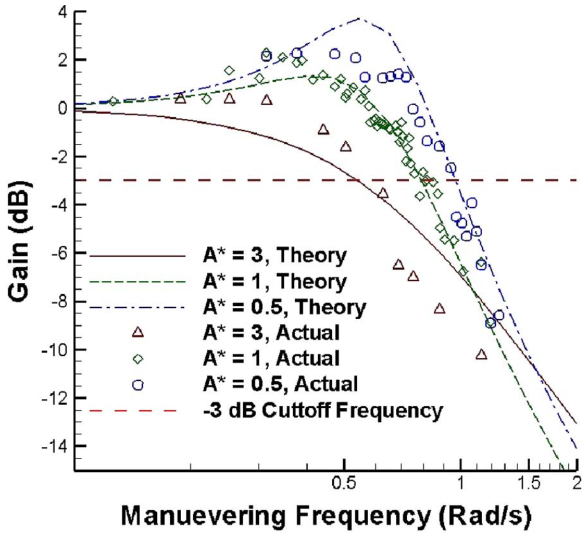

Fig. 14. Closed-loop frequency response for the thruster-vehicle system. *Cruising regime* shown by $A^\star = 3$, *Transition regime* shown by $A^\star = 1$, and *Docking regime* shown by $A^\star = 0.5$. Theoretical response modeled assuming $f_0 = 20$, 9, and 5 Hz, respectively.

including the cutoff frequency. A key parameter of the model linearization, which has not been discussed in detail, is the trim velocity, which is used to linearize the drag of the vehicle. This is one of the important parameters, which differentiates between the different maneuver regimes. In the *Docking regime*, the vehicle generally changes directions rapidly and spends much of its time at low velocities. Therefore, selecting the trim velocity according to a maximum-acceleration relation yields very good results and is an appropriate approximation. By contrast, the *Cruising regime* is characterized by long periods of sustained motion and the corresponding trim velocity should be set according to a velocity-drag relation. Although the transfer model for this regime predicts a cutoff close to the actual cutoff seen in the system, it incorrectly predicts the gain on either side of the cutoff frequency. This is because of the fact that maneuvers in the cruising regime experience drastically variable drag forces, since the drag force is nonlinear, and the vehicle has a larger velocity range in the cruising regime. Because of the nonlinearities and the sizable velocity range, the linearization about a single trim velocity predicts a drag, which is too large in the low frequency maneuvers, and similarly predicts a drag, which is too low for high frequency maneuvers. Therefore, the accuracy of the drag approximation will decrease as the maneuver scale increases. This implies that the large velocity range in the *Cruising regime* requires a sliding model to accurately predict system frequency response (as opposed to the small scale maneuvers, which are well approximated by a single trim velocity). Additionally, the model has no limitation on thrust level and, in this regime, drives the thruster beyond its actual capacity (even with relatively low gains). Although this is an unmodeled nonlinear effect, it also addresses an interesting design consideration. This analysis demonstrates that any high-accuracy thruster may not have a large enough range to be completely effective in the *Cruising regime*. The thruster could be designed with a larger output, but this would reduce the accuracy of the system in the *Docking regime*. Fortunately, maneuvers in the high frequency *Cruising regime* are also generally coupled with significant forward vehicle velocity. This strong cross flow gives the thrusters an added dimensionality, and instead of generating control forces strictly from the jetting momentum transfer, the VRT can be used to inject energy into the flow going over the vehicle, altering the effective shape of the vehicle seen by the surrounding flow. Furthermore, the effect of so-called "hydroshaping" increases with increased velocity, where the thrust generation is observed to be lacking. Aeroshaping has been shown to be an effective technique in fighter jets and general drag reduction [32]. Future studies will investigate the use of VRTs for the purpose of flow control.

VII. DISTURBANCE REJECTION

It should be noted that the maneuver frequency response analysis was performed, assuming that the vehicle was in a perfectly calm fluid environment. In reality, marine environments are characterized by oceanic currents of various amplitudes and frequencies. These disturbances from fluid currents can have a large effect on the trajectory of the vehicle (especially in the *Docking* regime). Unfortunately, the fluid velocity is a difficult quantity to measure, without affecting the external drag profile of the vehicle. External anemometers must be located at a sufficient distance from the vehicle to get accurate measurements, which is inherently coupled with a large drag moment. Adding to the complexity, the inertial velocity of the vehicle can also be very difficult to determine. Typical sensors like Doppler sensors and sonar arrays do not guarantee high-accuracy velocity sensing (especially at low velocities), and numerical differentiation of the position data will often lead to chattering in the control input, which drastically increases energy consumption and decreases total thruster lifespan [33].

One way to account for the fluid velocity is to define it as a state variable of the system and describe the corresponding dynamics accordingly. Therefore, the fluid velocity will be estimated using an observer, which is easily defined in the spectral domain

$$\begin{aligned} U_f(s) &= \left(\frac{M}{C_2}s^2 + s\right)X(s) + \frac{1}{C_2}\hat{T}(s) \\ &= G_O(s)X(s) + \frac{1}{C_2}\hat{T}(s). \end{aligned} \tag{17}$$

The observer is, therefore, a function of the present system state (both position and thrust).

Using this estimate of the relative fluid velocity, a control law can be designed to decouple the vehicle system from the drag forces and simplify the dynamics previously observed. The new adapted-control law is described by

$$u = -C_2 u_f + K(\tilde{x} + T_D \dot{\tilde{x}}) \tag{18}$$

where $\tilde{x}$ is the error between the desired maneuver trajectory and the actual vehicle trajectory. A conceptual diagram of the error-feedback algorithm is depicted in Fig. 15.

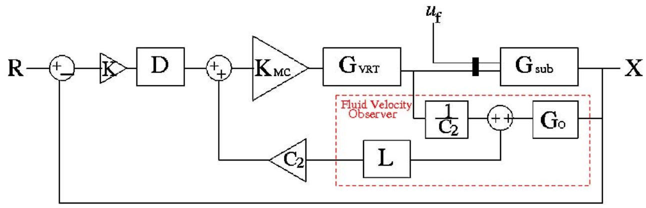

Fig. 15. Vehicle-feedback control block diagram. Fluid-velocity observer shown in dotted box.

There is an additional block in Fig. 15, which has yet to be discussed. The block labeled "L" is meant to represent a custom filter. It should be noted that the measurement of the state X, which is fed back into the fluid velocity observer is not the true state of the vehicle but contains measurement and electrical noise. Therefore, feeding the output of the observer through the low-pass filter will eliminate the fluid velocity component estimated because of measurement error [34], [35]. However, special care should be taken so that the filter cutoff frequency is not set too low with respect to the fluid environment, which would result in actual fluid disturbances being ignored as sensor noise. Consider an ocean environment near the surface, whose wave energy is described by the Pierson–Moskowitz spectrum [30]

$$S(\omega) = \frac{A}{\omega^5}\, e^{-B/\omega^4}. \tag{19}$$

In (19), A and B are constants defined by the wind velocity above the surface. Assuming a unitary wind velocity, this spectrum can be seen to have a corner frequency of approximately 0.75 rad/s. If a vehicle operating in this type of wave environment receives fluid velocity information from an observer of the type previously described, then the wave energy captured by the observer is directly linked to the cutoff frequency of the low-pass filter. Assume the low-pass filter shown in block L of Fig. 15 is a single first-order low-pass filter described by

$$L(s) = \frac{1}{1 + s\tau} \tag{20}$$

where τ is a time constant, which can be related to the filter cutoff frequency by $\tau = 0.4125/w_c$, where w_c is the –3 dB cutoff frequency). The ratio of total wave energy determined by the observer with respect to the total wave energy in the ocean environment is shown in Fig. 16. The total energy recovered is calculated by

$$E = \int_0^{w_c} S(\omega) d\omega. \tag{21}$$

The percentage of wave energy captured by the filter is then just E/E_0, where E_0 is the total energy (energy calculated from (21) with $w_c = \infty$).

If the vehicle designer wishes to capture 95% of the wave energy with the fluid velocity estimator, it can be seen from Fig. 16 that the low-pass filter cutoff frequency should be set to approximately 8 rad/s. This filter cutoff frequency corresponds to about ten times the fluid environment corner frequency. Using this parameter as an observer-design criterion should provide adequate fluid velocity estimation, as well as signal noise attenuation, since signal noise will typically be in the kilohertz range. Here, it should be noted that the fluid velocity observer architecture was laid out in the spectral domain, because of the simplicity of implementation/calculation, as well as the simple inclusion of the low-pass filter to eliminate noise. This should be adequate for the majority of operating schemes, since the spectral approximation of the vehicle dynamics were shown to be sufficiently accurate in Section VI-A and B. However, if the computation capabilities of the vehicle permit, the observer scheme can be reformatted in the time domain, as shown in the control algorithm of [33]. This architecture may be more useful in the *Docking Regime*, where the LTI approximation was seen to be less accurate, and the more accurate time-dependent thruster description of (4) can be incorporated. However, special care must be taken to insure proper signal noise filtering.

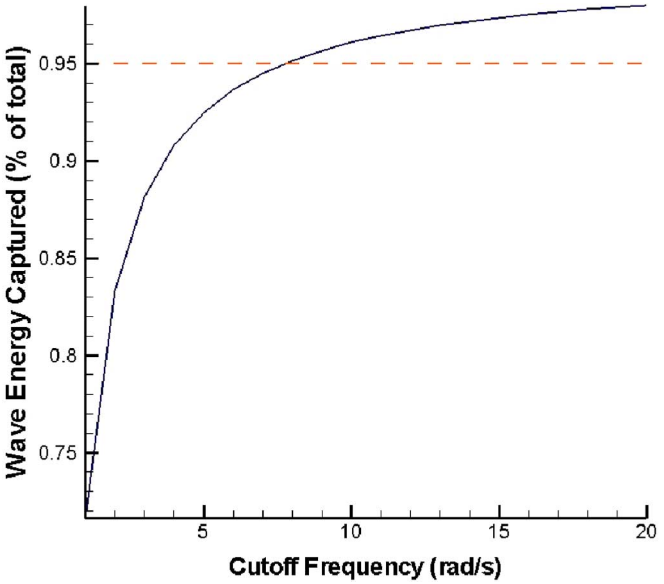

Fig. 16. Amount of wave energy determined by observer with respect to low-pass filter-cutoff frequency.

VIII. Future Work

Our group has developed two generations of underwater vehicles to house these thrusters and demonstrate their feasibility. These vehicles are shown in Figs. 17 and 18. As can be seen from these figures, the use of internal VRTs allows for a hydrodynamic low drag vehicle (excluding KRAKEN's nose, which was made flat to allow visual access for the front facing camera) with few protruding parts and no control surfaces whatsoever. These vehicles were quite successful as technology demonstrators and were both used to perform complicated maneuvers like zero-radius turning, pure sideways translation, and parallel parking maneuvers. A simulated parking maneuver performed autonomously by the second vehicle (KRAKEN) is shown in Fig. 19. The first frame shows the vehicle approaching the parking structure, the second frame shows the AUV translating into position, and the third frame shows the AUV

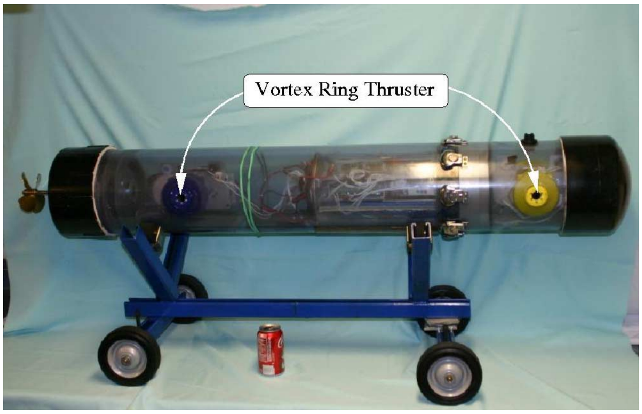

Fig. 17. CALAMAR-E: First-generation technology demonstrator.

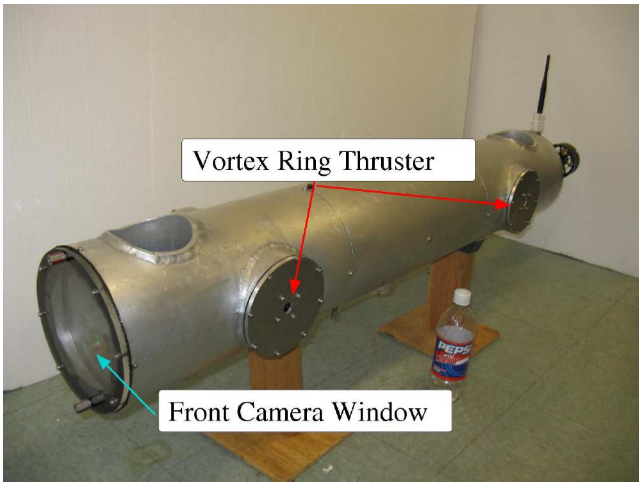

Fig. 18. KRAKEN: Second-generation vehicle, designed for use in competition.

hovering in a stationary position as determined by the image recognition system. For more information on this vehicle and its sensing capabilities, see [36]. KRAKEN was also entered in AUVSI's unmanned underwater vehicle competition, where it received an award for the "Best New Entry." However, in both cases, the thrusters were controlled using primitive feedforward algorithms. The level of high-accuracy maneuver required for an AOSN will require much more accurate control algorithms. Therefore, future control algorithms for these vehicles will incorporate the spectral thruster model of this paper, as well as the disturbance rejection algorithm in a 6-DOF architecture.

So far, the thrust analysis of these thrusters assumes that the exit nozzle remains rigidly fixed throughout pulsation. Future investigations will analyze the effect of a variable-diameter nozzle (which is found in the natural locomotion of squid and jellyfish). The results from an initial round of testing performed with a variable-diameter nozzle can be found in [37]. Additionally, the power and efficiency were unmeasured in this study, which was primarily performed to prove feasibility; future studies will explicitly classify VRT propulsive efficiency and power consumption, and compare with commercially available thrusters.

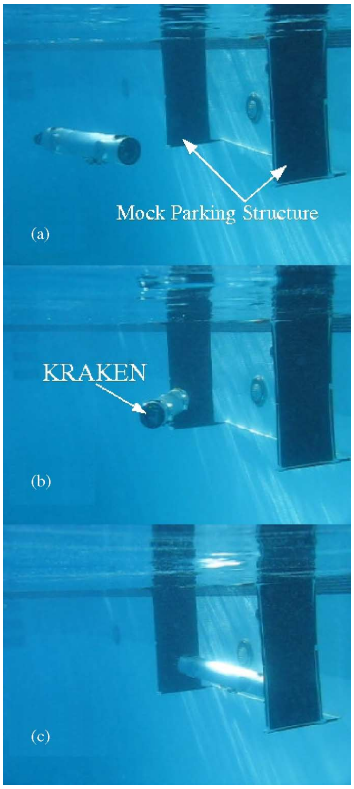

Fig. 19. KRAKEN performing a simulated parking/docking maneuver. (a) Moving into position. (b) Sideways translation into parking structure. (c) Stationary hover in parking position. A video of this maneuver can be found at http://enstrophy.colorado.edu/∼mohseni/videos/KRAKEN-AutonomousParallelParkAug2008a.avi.

IX. CONCLUSION

High-accuracy maneuvers are a pressing concern for underwater robotics, since the inclusion of maneuvering thrusters almost always results in a loss of long range transit capabilities. A new type of thruster inspired by cephalopod locomotion offers promising results for solving this problem. The thruster generates a pulsatile thrust by ingestion of surrounding fluid into an internal cavity and ejection of that fluid in the form of a high momentum vortex ring. Since the cavity is internal to the vehicle with only a small orifice making contact with the external flow, the thruster has almost no effect on the forward drag of the vehicle. A slug model was derived to predict the steady state thrust of the device, in terms of jet and thruster parameters. The slug model was determined to be accurate within a range of operational parameters (below the jet-formation number). This model was expanded upon to fully characterize the time dependent thrust as well. Additionally, a linear transfer function model was developed to approximate the transient dynamics of the thruster-vehicle assembly. Vehicle maneuvers were characterized in three different maneuver regimes based on this linearization, including the *Cruising, Docking*, and *Transition regimes*. This transfer function model was seen to accurately predict the frequency response of the system (both open and closed loop), with regard to the cutoff frequency and general shape of the frequency response, even though it ignores certain high order dynamics.

REFERENCES

[1] L. Whitcomb, D. Yoerger, H. Singh, and D. Mindell, “Towards precision robotic maneuvering survey, manipulation in unstructured undersea environments,” in *Proc. 8th Int. Symp.,* Y. Shirai and S. Hirose, Eds. London, U.K.: Springer-Verlag, 1998.

[2] D. Yoerger, J. Cooke, and J.-J. Slotine, “The influence of thruster dynamics on underwater vehicle behavior and their incorporation into control system design,” *IEEE J. Ocean. Eng.*, vol. 15, no. 3, pp. 167–178, Jul. 1990.

[3] M. Mclean, “Dynamic performance of small diameter tunnel thrusters,” Ph.D. dissertation, Naval Postgrad. School, Monterey, CA, 1991.

[4] H. Singh, J. Bellingham, F. Hover, S. Lemer, B. Moran, K. von der Heydt, and D. Yoerger, “Docking for and autonomous ocean sampling network,” *IEEE J. Ocean. Eng.*, vol. 26, no. 4, pp. 498–514, Oct. 2001.

[5] N. E. Leonard, D. A. Paley, F. Lekien, R. Sepulchre, D. M. Fratantoni, and R. E. Davis, “Collective motion, sensor networks, and ocean sampling,” *Proc. IEEE*, vol. 95, no. 1, pp. 48–74, Jan. 2007.

[6] J. Bellingham, C. Goudey, T. C. J. Bales, D. Atwood, J. Leonard, and C. Chryssostomidis, “A second generation survey AUV,” in *Proc. Symp. Auton. Underwater Vehicle Technol.*, Cambridge, MA, Jun. 1994, pp. 148–156.

[7] J. Bellingham and J. Wilcox, “Optimizing AUV oceanagraphic surveys,” in *Proc. IEEE Auton. Underwater Vehicle Technol.,* Monterey, CA, Jun. 2–6, 1996, pp. 391–398.

[8] R. O’ Dor, H. Portner, and R. Shadwick, *Squid as Elite Athletes: Locomotory, Respiratory and Circulatory Integration*. New York: Plenum, 1990, ch. 22, pp. 481–503.

[9] S. Neill and J. Cullen, “Experiments on whether schooling by their prey affects the hunting behavior of cephalopods and fish predators,” *J. Zool. Lond.*, vol. 172, pp. 549–569, 1974.

[10] D. Chen, G. Dykhuizen, J. Hodge, and W. Gilly, “Ontogeny of copepod predation in juvenile squid (loligo opalescens),” *Biol. Bull.*, vol. 190, pp. 69–81, 1995.

[11] M. Sahin and K. Mohseni, “An arbitrary Lagrangian–Eulerian formulation for the numerical simulation of flow patterns generated by the hydromedusa Aequorea victoria,” *J. Comput. Phys.*, vol. 228, pp. 4588–4605, 2009.

[12] M. Sahin, K. Mohseni, and S. Colins, “The numerical comparison of flow patterns and propulsive performances for the hydromedusae Sarsia tubulosa and Aequorea victoria,” *J. Exp. Biol.*, vol. 212, pp. 2656–2667, 2009.

[13] D. Lipinski and K. Mohseni, “A numerical investigation of flow structures and fluid transport with applications to feeding for the hydromedusae Aequorea victoria and Sarsia tubulosa,” *J. Exp. Biol.*, vol. 212, pp. 2436–2447, 2009.

[14] A. Glezer and M. Amitay, “Synthetic jets,” *Ann. Rev. Fluid Mech.*, vol. 34, pp. 503–529, 2002.

[15] K. Mohseni, “Pulsatile jets for unmanned underwater maneuvering,” presented at 3rd AIAA Unmanned Unlimited Tech. Conf., Workshop Exhib., Chicago, IL, Sep. 20–23, 2004, AIAA Paper 2004-6386.

[16] A. Polsenberg-Thomas, J. Burdick, and K. Mohseni, “An experimental study of voice-coil driven synthetic jet propulsion for underwater vehicles,” in *Proc. MTS/IEEE OCEANS*. Washington, DC, Sep. 19–23, 2005.

[17] K. Torsiello, “Acoustic positioning of the nps autonomous underwater vehicle (auv ii) during hover conditions,” Master’s thesis, Naval Postgrad. School, Monterey, CA, Mar. 1994.

[18] M. Dunbabin, J. Roberts, K. Usher, G. Winstanley, and P. Corke, “A hybrid auv design for shallow water reef navigation,” in *Proc. IEEE Int. Conf. Robot. Autom.*, Barcelona, Spain, Apr. 2005, pp. 2105–2110.

[19] S. Licht, V. Polidoro, M. Flores, F. Hover, and M. Triantafyllou, “Design and projected performance of a flapping foil auv,” *IEEE J. Ocean. Eng.*, vol. 29, no. 3, pp. 786–794, Jul. 2004.

[20] S. Licht, “Biomimetic oscillating foil propulsion to enhance underwater vehicle agility and maneuverablity,” Ph.D. dissertation, Mass. Inst. Technol., Cambridge, MA, 2008.

[21] Minirover remotely operated vehicle system. (2008). Teledyne Benthos, North Falmouth, MA, Tech. Rep., [Online]. Available: www.benthos.com

[22] Stingray remotely operated vehicle system. (2004). Teledyne Benthos, North Falmouth, MA, Tech. Rep., [Online]. Available: www.benthos.com

[23] H. H. Wang, S. M. Rock, and M. J. Lee, “Otter: The design and development of an intelligent underwater robot,” *Auton. Robots*, vol. 3, no. 2–3, pp. 297–320, 1996.

[24] G. Antonelli, S. Chiaverini, N. Sarkar, and M. West, “Adaptive control of an autonomous underwater vehicle: Experimental results on odin,” *IEEE Trans. Control Syst. Technol.*, vol. 9, no. 5, pp. 756–765, Sep. 2001.

[25] M. Krieg and K. Mohseni, “Thrust characterization of pulsatile vortex ring generators for locomotion of underwater robots,” *IEEE J. Ocean. Eng.*, vol. 33, no. 2, pp. 123–132, Apr. 2008.

[26] K. Mohseni, “Pulsatile vortex generators for low-speed maneuvering of small underwater vehicles,” *Ocean. Eng.*, vol. 33, no. 16, pp. 2209–2223, 2006.

[27] M. Gharib, E. Rambod, and K. Shariff, “A universal time scale for vortex ring formation,” *J. Fluid Mech*, vol. 360, pp. 121–140, 1998.

[28] K. Mohseni and M. Gharib, “A model for universal time scale of vortex ring formation,” *Phys. Fluids*, vol. 10, no. 10, pp. 2436–2438, 1998.

[29] T. I. Fossen, “Nonlinear modelling and control of underwater vehicles,” Ph.D. dissertation, Norwegian Inst. Technol., Trondheim, Norway, 1991.

[30] W. Pierson and L. Moskowitz, “Proposed spectral form for fully developed wind seas based on the similarity theory of S. A. Kitaigorodskii,” *J. Geophys. Res.*, vol. 69, no. 3, pp. 5181–5190, 1964.

[31] P. Krueger, J. Dabiri, and M. Gharib, “The formation number of vortex rings formed in a uniform background co-flow,” *J. Fluid Mech.*, vol. 556, no. 1, pp. 147–166, 2006.

[32] M. Amitay, D. R. Smith, V. Kibens, D. Parekh, and A. Glezer, “Aerodynamic flow control over an unconventional airfoil using synthetic jet actuators,” *AIAA J.*, vol. 39, no. 3, pp. 361–370, 2001.

[33] G. Antonelli, F. Caccavale, S. Chiaverini, and L. Villani, “Tracking control for underwater vehicle manipulator systems with velocity estimation,” *IEEE J. Ocean. Eng.*, vol. 25, no. 3, pp. 399–413, Jul. 2000.

[34] G. Chung, K. Eom, B. Yi, I. Suh, S. Oh, and Y. Cho, “Disturbance observer-based robust control for underwater robotic systems with passive joints,” in *Proc. IEEE Int. Conf. Robot. Autom.*, San Fransisco, CA, Apr. 2000, pp. 1775–1780.

[35] H. Lee, “Robust digital tracking controllers for high-speed/high-accuracy positioning system,” Ph.D. dissertation, Univ. California, Berkeley, 1994.

[36] T. Clark, P. Klein, G. Lake, S. Lawrence-Simon, J. Moore, B. Rhea-Carver, M. Sotola, S. Wilson, C. Wolfskill, and A. Wu, “Kraken: Kinematically roving autonomously kontrolled electro-nautic,” in *AIAA Aerosp. Sci. Meeting*, Cambridge, MA, Jan. 2009.

[37] T. Thomas, M. Krieg, and K. Mohseni, “Thrust characterization for bio-inspired pulsatile vortex ring thrusters with variable exit nozzle diameter,” presented at the ASME Int. Mech. Eng. Congr. Expo., Buena Vista, FL, Nov. 13–19, 2003.

Michael Krieg (S’07) received the B.S. degree in aerospace engineering sciences from the University of Colorado at Boulder, Boulder, where he is currently working toward the Ph.D. degree.

His current research interests include hydrodynamic design, multiple-vehicle cooperative control, and novel propulsive schemes.

Kamran Mohseni (M’08) received the B.S. degree from the University of Science and Technology, Tehran, Iran, the M.S. degree in aeronautics from the Imperial College of Science, Technology, and Medicine, London, U.K., and the Ph.D. degree in mechanical engineering from the California Institute of Technology (Caltech), Pasadena, in 2000.

He was a Postdoctoral Fellow in control and dynamical systems with Caltech. In 2001, he joined the University of Colorado at Boulder, where he is currently an Associate Professor in aerospace engineering sciences. His research interests include mobile sensor networking platforms, microscale transport, vortex dynamics, and biomimetic and fluidic locomotion.

Dr. Mohseni is a member of the American Society of Mechanical Engineers, the American Physical Society, and the Society for Industrial and Applied Mathematics. He is an Associate Fellow of the American Institute of Aeronautics and Astronautics.